Electrochimica Acta 404 (2022) 139598

Contents lists available at ScienceDirect

Electrochimica Acta

journal homepage: www.elsevier.com/locate/electacta

Electron-transfer enhanced sponge-like CrP-Re_2P as a robust bifunctional electrocatalyst for high-current overall water splitting and Zn–H_2O cell

Lixia Wang[a], Zhiyang Huang[a], Hexiu Huang[a], Shenghong Zhong[b,*], Meilin Huang[a], Tayirjan Taylor Isimjan[c,*], Xiulin Yang[a,*]

[a] Guangxi Key Laboratory of Low Carbon Energy Materials, School of Chemistry and Pharmaceutical Sciences, Guangxi Normal University, Guilin 541004, China
[b] Key Laboratory of Advanced Materials Technologies (Fuzhou University), College of Materials Science and Engineering, Fuzhou University, Fuzhou 350108, China
[c] Saudi Arabia Basic Industries Corporation (SABIC) at King Abdullah University of Science and Technology (KAUST), Thuwal, 23955-6900, Saudi Arabia

ARTICLE INFO

Article history:
Received 9 August 2021
Revised 7 November 2021
Accepted 13 November 2021
Available online 16 November 2021

Keywords:
CrP-Re_2P
Bifunctional
Synergistic effect
Overall water splitting
Zn–H_2O cell

ABSTRACT

Developing dual functions, high-performance and stable catalysts for simultaneous hydrogen evolution reaction (HER) and oxygen evolution reaction (OER) at high-current density is highly desirable but still remaining as a challenge. Herein, a porous sponge-like structure of CrP-Re_2P composite was successfully constructed on nickel foam (NF) via a facile hydrothermal, drop casting, and subsequent phosphating treatment. Remarkably, the CrP-Re_2P/NF exhibits extraordinary performance with an ultralow overpotential of 148 mV at a current density of 100 mA cm^{-2} for HER and 255 mV at 20 mA cm^{-2} for OER in 1.0 M KOH, respectively. In addition, the bifunctional catalyst also manifests high-efficiency overall water splitting performance that drives a two-electrode system with 500/1000 mA cm^{-2} at a voltage as low as 1.89/2.02 V in 30% KOH. Moreover, the overall water-splitting device can achieve superior durability for 100 h at a current density of 100 mA cm^{-2} without obvious degradation. More significantly, the CrP-Re_2P/NF is used as the cathode of alkaline Zn-H_2O cell with a power density of 8.8 mW cm^{-2} and robust stability for 180 h, indicating that the catalyst has an encouraging industrial perspective. The excellent electrocatalytic performance of CrP-Re_2P/NF is mainly attributed to the porous structure exposing more active sites, high conductivity resulted better charge transfer, as well as the strong synergy between CrP and Re_2P species to regulate the binding energy with reactant intermediates. The strategy provides a novel and feasible approach for the development of highly efficient and stable bifunctional catalysts for overall water splitting and Zn–H_2O cell.

1. Introduction

At present, the over-exploitation and use of traditional fossil fuels have caused serious environmental problems and energy crises [1,2]. As a result, exploring renewable energy-based alternatives has been attracted a lot of attentions [3,4]. Electrochemical water splitting to produce clean hydrogen fuel is considered to be one of the most effective and competitive methods to obtain green energy [5,6]. Hence, it is urgent to develop an efficient and stable catalyst to decrease the over-potentials of hydrogen evolution (HER) and oxygen evolution (OER) reactions [7]. The state-of-art HER and OER catalysts are mainly are noble metals-based [8]. Nevertheless, the high costs, scarcity, and lower stability markedly impede their practical applications [9]. Therefore, it is indispensable to develop cheap, effective and stable noble metal-free electrocatalysts applicable at large current density (200–400 mA cm^{-2}) [10,11]. However, it is a challenging task.

Compared to neighbor *d*-metals (Ni, Fe, Co, Cu, and Zn) that have been extensively investigated the HER and OER catalysts [12,13], not many works have been done on chromium-containing electrocatalysts [14] despite the unique features. For example, as a group VI transition metal, the *d*-orbital of chromium has a strong adsorption strength for molecular substances and promotes the release of electrocatalytic hydrogen [15]. Moreover, Cr^{3+} cations exhibit a special electronic structure (t^3_{2g} e^0_g) that facilitates electron transfer and electron capture [16]. Besides, chromium is one

* Corresponding authors.
E-mail addresses: shenghong.zhong@fzu.edu.cn (S. Zhong), isimjant@sabic.com (T.T. Isimjan), xlyang@gxnu.edu.cn (X. Yang).

https://doi.org/10.1016/j.electacta.2021.139598
0013-4686/

of the cheapest transition metals. However, chromium alone cannot act as efficient HER/OER catalyst, therefore, it is often combined with other transition metals. For instance, Lin et al. reported a $Cr_{0.6}Ru_{0.4}O_2$ with remarkable OER performance in the acidic condition that has a low overpotential of 178 mV at 10 mA cm^{-2} [17]. Lin et al. reported a series of $Co_{2.25}Cr_{0.75}O_4$ catalysts via thermal decomposition, explored the OER performance, and achieved a mass activity of 10.5 A/g at 0.35 V overpotential at 10 mA cm^{-2} [18]. Recently, Li et al. revealed a Co_2Cr_1-P@3DGF highly efficient and durable bifunctional electrocatalyst for water electrolysis in a 1.0 M KOH which requires 118 and 270 mV to afford 10 mA cm^{-2} [19], respectively. Additionally, the two electrodes overall water splitting in alkaline media demands a cell voltage of 1.56 V at 10 mA cm^{-2}. The positive impact of phosphate treatment towards HER/OER performance of chromium based electrocatalyst also revealed in other studies as well [20]. Nevertheless, most of those studies focused on low current density (10 mA cm^{-2}) which is not applicable to the industrial process. In light of these successful stories and our previous experience [21,22], we propose to design chromium-rhenium-phosphor bifunctional electro-catalyst at high current density (>100 mA cm^{-2}). The *Re* is selected in this study owing to its exceptional plasticity, and corrosion resistance [23]. In addition, there are some previous reports on outstanding electrocatalytic performances of rhenium sulfides [24,25], rhenium oxides [26], and rhenium-doped compounds [27]. Although rhenium is the cheapest noble metal (the cost of the *Re* is almost 1/6 of the Pt), the price of a purely *Re* catalyst is still high [28]. Therefore, it is necessary to dilute the *Re* content using Cr to cut the cost.

In this work, we coupled CrP with Re_2P components together on NF to obtain CrP-Re_2P/NF with a sponge-like porous structure. A variety of characterization techniques are used to characterize the crystal structure, microscopic morphology, chemical state and content. Electrochemical studies have confirmed that the CrP-Re_2P/NF catalyst has excellent bifunctional electrocatalytic activity and stability in 1.0 M KOH in terms of HER and OER. The overall water splitting result indicated that the CrP-Re_2P/NF $^{(+/-)}$ bifunctional catalyst has superior catalytic performance in a two-electrode electrolyzer at high current density comparable to the state-of-the-art catalyst system Pt/C/NF $^{(-)}$‖RuO_2/ NF $^{(+)}$. Moreover, the Zn-H_2O cell using CrP-Re_2P/NF as the cathode also shows high power density (8.8 mW cm^{-2}) and robust stability (180 h). To the best of our knowledge, this is the first detailed study highlighting the practical applications of Cr-*Re* based bimetallic catalysts.

2. Experimental

2.1. Materials

Chromic nitrate ($Cr(NO_3)_3 \cdot 9H_2O$, ≥99%), urea, ammonium perrhenate (NH_4ReO_4, >99.999%), ethanol absolute (C_2H_5OH, ≥99.7%), Nafion (5% solution), sodium hypophosphite monohydrate ($NaH_2PO_2 \cdot H_2O$, 99%), and potassium hydroxide (KOH) were purchased from Guangxi Zoey Biotechnology Co., Ltd. All reagents are analytical grade and were used without further purification. Commercial Pt/C (20 wt% for platinum) was purchased from Alfa Aesar. The Ni foam (NF) substrate used in the experiments has the thickness of 1.5 mm and 3 cm × 3 cm the area.

2.2. Catalyst synthesis

2.2.1. Preparation of CrOOH/NF precursor

The NF was sonicated successively with 0.5 M H_2SO_4, deionized water and ethanol for 15 min to remove impurities. In a typical synthesis, $Cr(NO_3)_3 \cdot 9H_2O$ (2.5 mmol) and $CO(NH_2)_2$ (25 mmol) were dissolved in 80 mL of deionized water and stirred for 15 min to obtain a clear solution. Then the resulting solution was transferred into a 100 mL Teflon-line stainless steel autoclave. The pretreated NF (3 cm × 3 cm) was placed obliquely in the autoclave and kept at 120 °C for 12 h. After cooling to room temperature naturally, the obtained product was washed with deionized water for several times and dried at room temperature for further use. In order to optimize the influence of hydrothermal time, CrOOH-10/NF, CrOOH-14/NF were also prepared under the same conditions but different processing times (10 h and 14 h).

2.2.2. Synthesis of Cr-Re species

NH_4ReO_4 (0.15 mmol) was dissolved in a mixed solution containing 200 μL deionized water, 200 μL ethanol and 10 μL Nafion and ultrasonicated for 20 min. The Nafion is used as a binding agent [29]. Then the mixture solution was pipetted onto the surface of CrOOH/NF (1 cm × 1 cm) to obtain the Cr-*Re* species/NF. For comparison, the Cr-*Re* species/NF with different *Re* loadings were prepared under the same condition by varying the NH_4ReO_4 molar content (0, 0.05, 0.1, 0.2 mmol).

2.2.3. Synthesis of CrP-Re_2P/NF

Two pieces of Cr-*Re* species/NF (1 cm × 1 cm) and 1.0 g of $NaH_2PO_2 \cdot H_2O$ were placed on the downstream and upstream of the tube furnace, respectively. Subsequently, the tube furnace was heated slowly to 350 °C (5 °C min^{-1}) under N_2 flow (20 sccm) for 2 h. After natural cooling to room temperature, the yellow phosphate formed at the top of the quartz tube adhered to the surface of the catalysts (Fig. S1), therefore the catalysts were washed with deionized water to get rid of the phosphate contaminate. The prepared sample was named as CrP-Re_2P/NF. For comparison, CrP/NF and Re_2P/NF were synthesized using similar procedure as CrP-Re_2P/NF. The catalyst loading of the CrP-Re_2P, CrP, and Re_2P on NF surface are approximately 24.4, 24.2 and 18.6 mg cm^{-2}, respectively, and are summarized in Table S1.

Moreover, CrO_3/NF, ReO_2/NF and CrO_3-ReO_2/NF were also synthesized under similar conditions without phosphatization process.

2.2.4. Synthesis of Pt-C/NF and RuO_2/NF

Pt/C/NF and RuO_2/NF electrodes were fabricated via a typical method. Briefly, 2 mg of commercial Pt/C (20 wt%) and 2 mg of RuO_2 were dispersed in a mixture solution of 200 μL ethanol, 200 μL water and 10 μL Nafion to form homogeneous solution, respectively. After that, the mixture was pipetted onto the surface of NF (1 cm × 1 cm) and dried in the air naturally. The loading of Pt/C and RuO_2 on NF is about 2 mg cm^{-2}.

2.3. Electrochemical measurements

The electrochemical performance of the as-prepared catalyst was measured by the electrochemical workstation of Bio-logic VMP3, using a conventional three-electrode system in 1.0 M KOH at room temperature. Catalyst was used as the working electrode, a graphite plate served as the counter electrode, and a saturated calomel electrode (SCE) was the reference electrode. The obtained catalysts were electrochemically pre-activated by cyclic voltammetry (CV) tests for about 5 cycles at a scan rate of 5 mV s^{-1} to make the catalysts reach a stable state. Linear sweep voltammetry (LSV) measurement was carried out at a scan rate of 5 mV s^{-1} for HER performance, and 0.2 mV s^{-1} for OER performance, the lower OER sweep rate was used as compared to the HER to reduce the oxidation peak resulted from Ni oxidation during the test. Electrochemical impedance spectroscopy (EIS) was conducted in the frequency range from 200 kHz to 10 MHz. In this work, all potentials (vs. SCE) have been corrected by the average CV curve of the two potentials, where the current value through zero point (1.040 V) is regarded as the thermodynamic potential of 1.0 M KOH with H_2-saturated

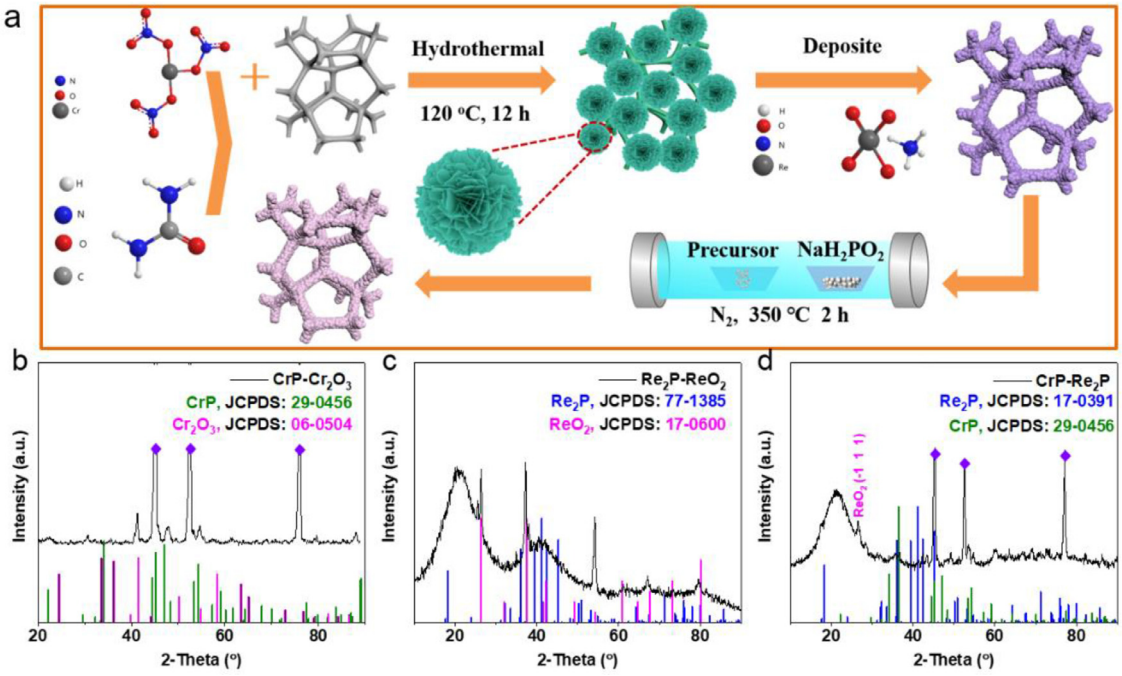

Fig. 1. (a) Schematic illustration of the preparation of CrP-Re_2P/NF. (b) XRD patterns of CrP, (c) Re_2P powder, and (d) CrP-Re_2P/NF. Note: Re_2P powder was scraped from the surface of NF.

for about 10 min (Fig. S2a). The potential (vs. SCE) of the long-term stability test and the overall water splitting test in 30% KOH were also corrected by the average CV curve of the two potentials. Current zero crossing (1.139 V) was regarded as the thermodynamic potential in 30% KOH (Fig. S2b). Overall water splitting test was performed in 1.0 M KOH and 30% KOH solution with a scan rate of 5 mV s^{-1}. The long-term stability test of the two electrodes system was measured at constant current density of 100 mA cm^{-2} in 30% KOH for 100 h. All the curves reported in this work have been calibrated by *iR* compensation, and all electrochemical tests were performed at room temperature (25 ± 1 °C).

2.4. Characterization

The morphology of the samples was analyzed by scanning electron microscopy (SEM, Quanta FEG 200, Holland) and transmission electron microscopy (TEM, JEOL, JEM-2100F). X-ray powder diffraction (XRD) data obtained through a D/Max 2500 V PC with Cu Kα radiation (Rigaku, USA). The actual loadings of various metals in the catalyst were detected by inductively coupled plasma mass spectroscopy (ICP-MS). X-ray electron spectrometer (XPS, model: JPS-9010 TR Photo-electron Spectrometer, Japan) was used to analyze the composition of surface elements and the valence states.

3. Results and discussion

3.1. Structural and morphological characterizations

The synthesis steps of CrP-Re_2P/NF were illustrated in Fig. 1a. In the first step, CrOOH/NF was synthesized by hydrothermal reaction in a stainless-steel autoclave at 120 °C for 12 h containing a cleaned NF (3 cm × 3 cm). In this process, the color of the nickel foam changes from metallic gray to green. Afterwards, the *Re* species was pipetted onto the surface of CrOOH/NF to obtain Cr-*Re* species/NF and a layer of white powder was attached to the green nickel foam. The target catalyst was obtained by phosphate treatment in a tube furnace at 350 °C for 2 h.

The phase chemical composition of catalysts was determined by X-ray diffraction (XRD). For CrOOH/NF precursor, the diffraction peaks of CrOOH powder are consistent with the standard diffraction pattern (JCPDS: 06-0160) [30], confirming that CrOOH/NF was successfully synthesized (Fig. S3). After phosphatization, the XRD revealed that the CrOOH component had been converted to CrP (JCPDS: 29-0456) [20], along with Cr_2O_3 (JCPDS: 15-0718) (Fig. 1b) [31]. A similar situation was also observed in Re_2P sample. In addition to some target diffraction peaks of Re_2P (JCPDS: 77–1385), the diffraction peaks of ReO_2 (JCPDS: 17-0600) were also detected (Fig. 1c) [23]. As shown in Fig. 1d the diffraction peaks of CrP-Re_2P/NF align with the CrP (JCPDS: 290,456) and Re_2P (JCPDS: 17-0391), indicating the two major crystalline structures are CrP and Re_2P. In addition, the XRD patterns of CrP-Re_2P obtained with different *Re* loadings are shown in Fig. S4. The inductively coupled plasma mass spectrometry (ICP-MS) was used to calculate the final composition of the catalyst because EDS and XPS reflect the surface compositions, which cannot be used for quantitative analysis. ICP-MS measured different catalysts loading are shown in Table S2. The chemical formulas of the CrP-Re_2P/NF catalysts with different *Re* loadings are summarized in Table S3.

The surface morphology of the prepared catalysts shows in (Fig. S5). The CrOOH/NF prepared by the hydrothermal *in-situ* growth method has different morphologies upon the reaction times, which can be categorized as bulk (10 h), flower-like (12 h), to porous structure (14 h). The surface of NF was covered with a large amount of loose and porous sponge-like materials, when the precursor of *Re* was loaded on the CrOOH/NF (12 h) surface and followed by phosphate treatment (Fig. 2a). TEM image of the ultrasonically stripped catalyst fragments shows that there are uniformly distributed nanoparticles on the surface of the flakes (Fig. 2b), and the average size of the particles is about 1.64 nm (inset Fig. 2b). The selected area electron diffraction (SAED) in Fig. 2c reveals that the lattice spacing of 0.203 nm and 0.181 nm correspond to the CrP (210) and Re_2P (114) crystal planes, confirming that the catalyst is composed of CrP and Re_2P, which are consistent with the XRD results. The main components of the particles are at-

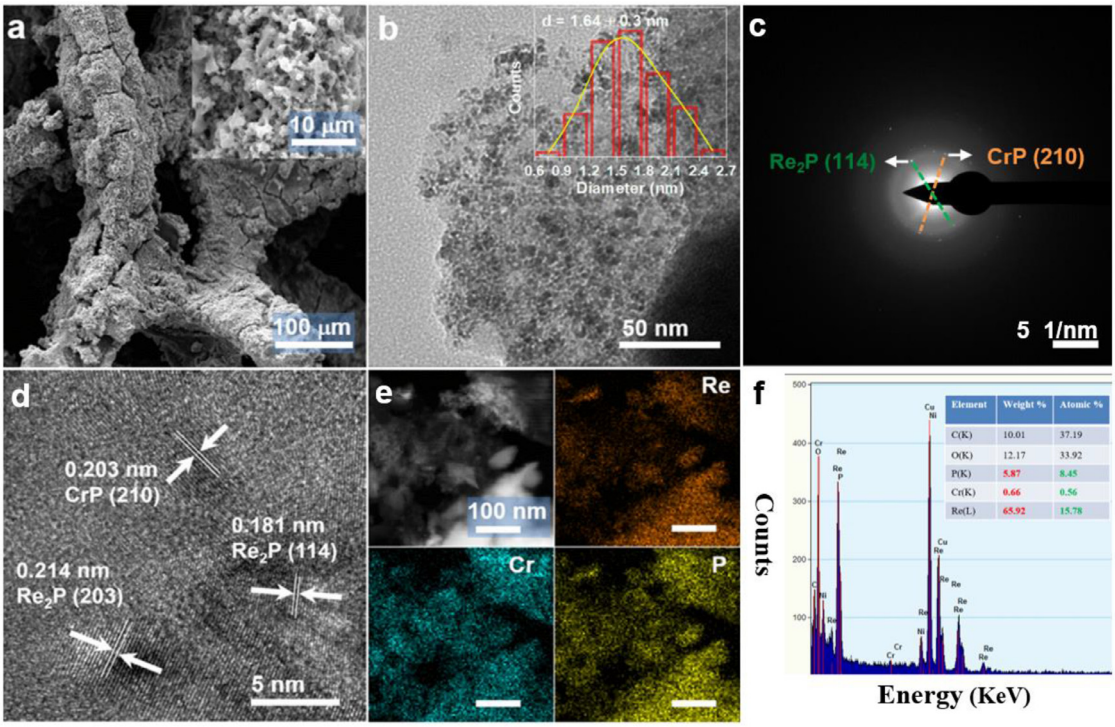

Fig. 2. (a) SEM (inset of high-magnification), (b) TEM (inset of particle size distribution), (c) SAED of CrP-Re_2P/NF, (d) high-resolution TEM images, (e) HAADF-STEM image and corresponding element mappings of CrP-Re_2P/NF, and (f) EDS spectrum profile (inset of EDS data) of CrP-Re_2P/NF.

tributed to the (114) and (203) crystal planes of Re_2P species with lattice spacings of 0.181 and 0.214 nm (Fig. 2d). In addition, the (210) crystal plane of the CrP component with a lattice spacing of 0.203 nm was also observed. The high annular dark-field scanning TEM (HAADF-STEM) image and corresponding elemental mappings display that Cr, *Re* and P are uniformly distributed throughout the CrP-Re_2P/NF (Fig. 2e). Energy-dispersive X-ray spectrometer (EDS) analysis of CrP-Re_2P/NF catalyst is showed in Fig. 2f. The Ni peak is attributed to the nickel foam, and the O peak can be attributed to the oxidation of the catalyst surface when exposed to air, which is consistent with the XRD results. The Cr, *Re*, and P come from CrP-Re_2P/NF.

XPS measurement was used to elucidate the surface composition and chemical state of CrP-Re_2P/NF. The XPS indicated the surface compositions of Cr, *Re* and P elements in CrP-Re_2P/NF (Fig. S6a). The peak of Ni is attributed to nickel foam (NF). First, the high-resolution C 1 s spectrum is deconvoluted into three peaks, including C–C (284.8 eV), C–O (286.0 eV) and C=O (288.8 eV) and used as standards for correction (Fig. S6b) [32,33]. The high-resolution XPS spectra of Cr 2*p* of CrP-Re_2P/NF and CrP/NF are depicted in Fig. 3a. The Cr 2*p* region of CrP-Re_2P/NF presents three major groups, in which the deconvoluted peaks at 575.3 (Cr $2p_{3/2}$) and 584.6 (Cr $2p_{1/2}$) eV are attributed to Cr-P, the binding energies at 578.0 and 587.2 eV are assigned to Cr-O species, and the two peaks at 580.9 eV and 590.3 eV are ascribed to higher valence Cr oxides [20,34]. Deconvolution of high-resolution spectra in the *Re* 4*f* region shows the presence of the doublet *Re* $4f_{7/2}$ (41.6 eV) and $4f_{5/2}$ (43.4 eV) for CrP-Re_2P/NF (Fig. 3b) [24,25]. Besides, the other two sets of additional doublets *Re* $4f_{7/2}$ (44.0 & 48.8 eV) and $4f_{5/2}$ (46.2 & 48.5 eV) can be ascribed to various *Re* oxides [35,36]. Moreover, the high resolution XPS spectra of the P 2*p* core levels are displayed in Fig. 3c. The P 2*p* of CrP-Re_2P/NF mainly includes P 2 $p_{3/2}$ (129.6 eV) and P $2p_{1/2}$ (130.5 eV), which is obviously different from CrP/NF (129.1 eV for $2p_{3/2}$) and Re_2P/NF (128.7 eV for $2p_{3/2}$) [37,38]. The binding energy of Cr 2*p* in CrP/NF at 576.21 eV shows a positive shift compared to that of Cr metal (from 573.8 to 574.6 eV). Similarly, compared with *Re* metal (from 40.1 to 41.0 eV), the binding energy of *Re* 4*f* of Re_2P/NF at 41.1 eV also shows a positive shift. Besides, the P $2p_{3/2}$ binding energies of CrP/NF (129.2 eV) and Re_2P/NF (128.6 eV) show an obvious negative shift compared with element P (130.2 eV). This result shows that the elements Cr and *Re* in the single metal phosphides CrP/NF and Re_2P/NF have partial positive charges. In contrast, phosphorus has partial negative charges to transfer electrons from the metals Cr and *Re* to P [39]. Interestingly, the CrP $2p_{3/2}$ of CrP-Re_2P/NF has a negative shift of approximately 0.91 eV relative to that of CrP/NF. Notably, the peak position of *Re* 4*f* in CrP-Re_2P/NF showing a positive shift approximately 0.50 eV as compared to that of Re_2P/NF. The XPS peak intensity differences between the Cr (3*p*) and *Re* (4*f*) in CrP-Re_2P compared to those of CrP and Re_2P are the results of dilution of the single components and the indication of the substantial charge transfer between the CrP and Re_2P.The significant binding energy shifts CrP and Re_2P in CrP-Re_2P/NF suggesting possible electrons transfer between the two species resulted synergetic effect [40,41],which is responsible for the enhanced the catalytic activity of HER/OER discussed below [42].

3.2. Electrocatalytic performance

The electrocatalytic water splitting performance of CrP-Re_2P/NF together with CrP/NF, Re_2P/NF, Pt/C/NF, and RuO_2/NF in 1.0 M KOH solution were discussed below. Initially, the HER electrocatalytic performance of CrP-Re_2P/NF was optimized by changing the hydrothermal treatment time during the catalyst preparation process. The result illustrated that the catalyst with a hydrothermal reaction time of 12 h has the optimal HER activity and the smallest Tafel slope (Fig. S7). Secondly, the influence of NH_4ReO_4 precursors with different molar contents on the catalytic performance was also analyzed (Fig. S8), and found that the catalyst has the best performance when the *Re* loading was 0.15 mmol. Finally, we compared Cr and *Re* phosphides with the corresponding ox-

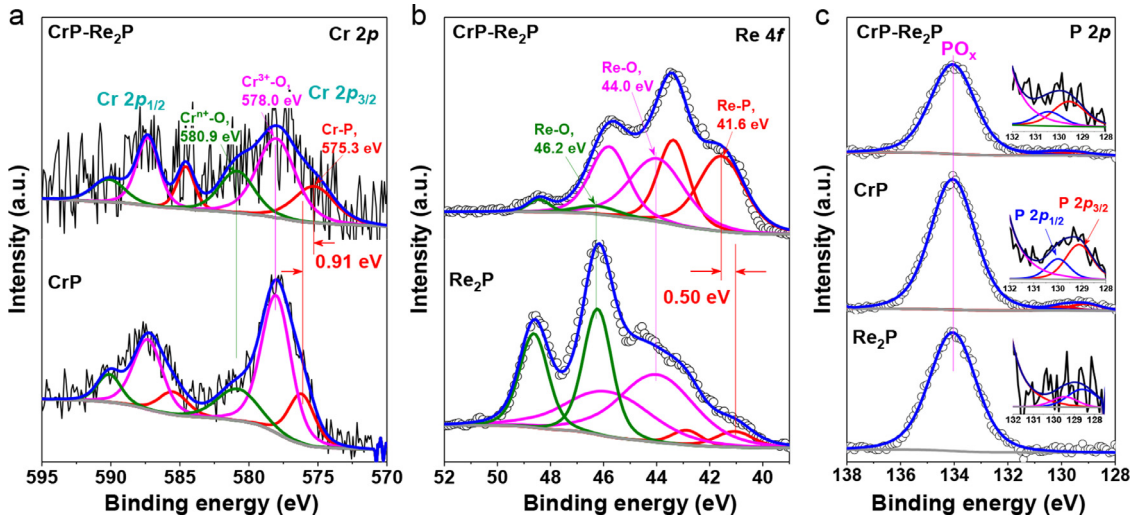

Fig. 3. (a) High-resolution XPS spectra of (a) Cr 2*p* of CrP-Re_2P/NF and CrP/NF, (b) *Re 4f* of CrP-Re_2P/NF and Re_2P/NF, and (c) P 2*p* of all samples.

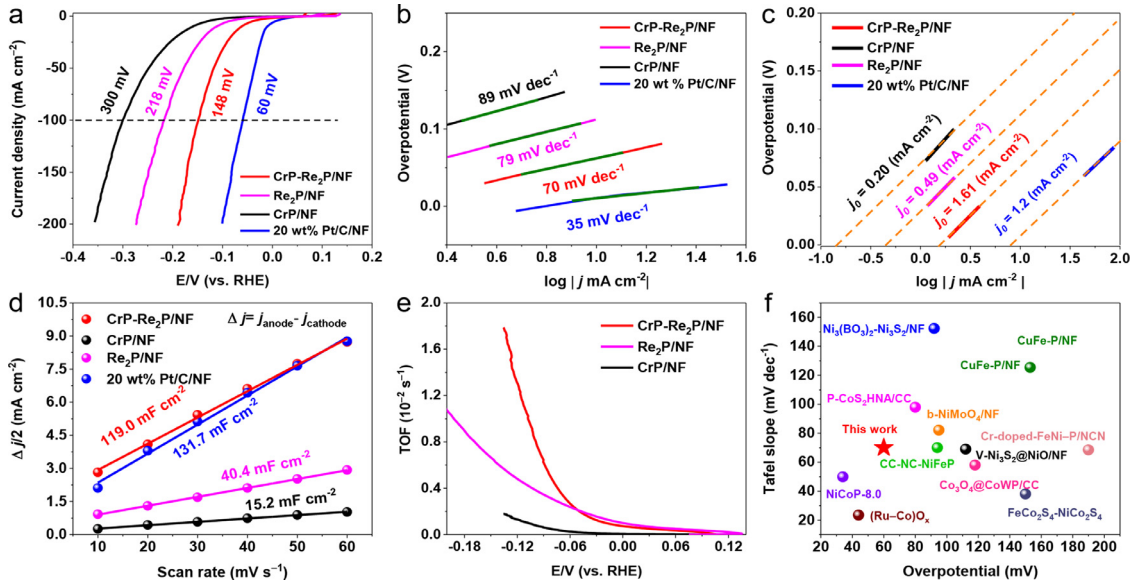

Fig. 4. HER performance of CrP-Re_2P/NF, CrP, Re_2P/NF and Pt/C in 1.0 M KOH. (a) LSV polarization curves, (b) corresponding Tafel slopes, (c) exchange current density, (d) double layer capacitance (C_{dl}), (e) turnover frequency (TOF) value, and (f) comparison with the overpotentials of recently reported catalysts for HER activity at 10 mA cm^{-2}.

ides. The results showed that the oxides have a minor influence on electrocatalytic performance under the same conditions, indicating the phosphatization step's importance (Fig. S9), even though the oxides account for about 50% CrP for about 25% on the surface (XPS). Fig. 4a displays the HER linear LSV polarization curve of various electrodes in 1.0 M KOH. CrP-Re_2P/NF demonstrates unprecedented performance for HER, it requires relatively low overpotential of 148 mV to reach the current density of 100 mA cm^{-2}, which is close to commercial Pt/C/NF (60 mV), while significantly superior as compare to CrP/NF (300 mV) and Re_2P/NF (218 mV). The catalyst showed a significant advantage in terms of mass current density. For example, at an overpotential of 100 mV, the mass current density of CrP-Re_2P/NF is approximately 5.4- and 9.3-fold that of Re_2P/NF and CrP/NF (Fig. S10a), respectively. The Tafel slope is commonly used to evaluate the reaction kinetics and rate determination steps in the HER process [43]. As shown in Fig. 4b, the Tafel slope of CrP-Re_2P/NF, CrP/NF, Re_2P/NF and Pt/C were calculated to be 70, 89, 79 and 35 mV dec^{-1}, respectively. Notably, the Tafel slope of CrP-Re_2P/NF is smaller than those of all control catalysts suggesting that the catalytic HER process obeys the Volmer-Hayrovsky mechanism, and the electrochemical desorption is the rate-determining step [44].

Moreover, the exchange current density (j_0) can reflect the intrinsic activity of the catalyst as well as the intrinsic electron transfer rate between the catalyst and the electrolyte [44]. As evidenced in Fig. 4c, the j_0 of CrP-Re_2P/NF is 1.61 mA cm^{-2}, which is larger than that of CrP/NF (0.20 mA cm^{-2}), Re_2P/NF (0.49 mA cm^{-2}) and Pt/C/NF (1.2 mA cm^{-2}), implying that CrP-Re_2P/NF has the best intrinsic catalytic activity. In general, the electrochemical double layer capacity (C_{dl}) is directly proportional to the ECSA of the catalyst [45]. The cyclic voltammetry (CV) curve can be used to calculate the C_{dl} of the non-faradaic potential range (Figs. S11–12). As shown in Fig. 4d, the C_{dl} value of CrP-Re_2P/NF is 119.0 mF cm^{-2}, which is higher than those of CrP/NF (15.2 mF cm^{-2}), Re_2P/NF (40.4 mF cm^{-2}), and close to commercial Pt/C/NF (131.7 mF cm^{-2}), indicating that CrP-Re_2P/NF has exposed more available active site. The turnover frequency (TOF) was calculated using ICP-MS results to further determine the intrinsic catalytic activity [46]. As shown in Fig. 4e, the TOF value of CrP-Re_2P/NF increased faster than that of CrP/NF and Re_2P/NF when the applied potential increases, sug-

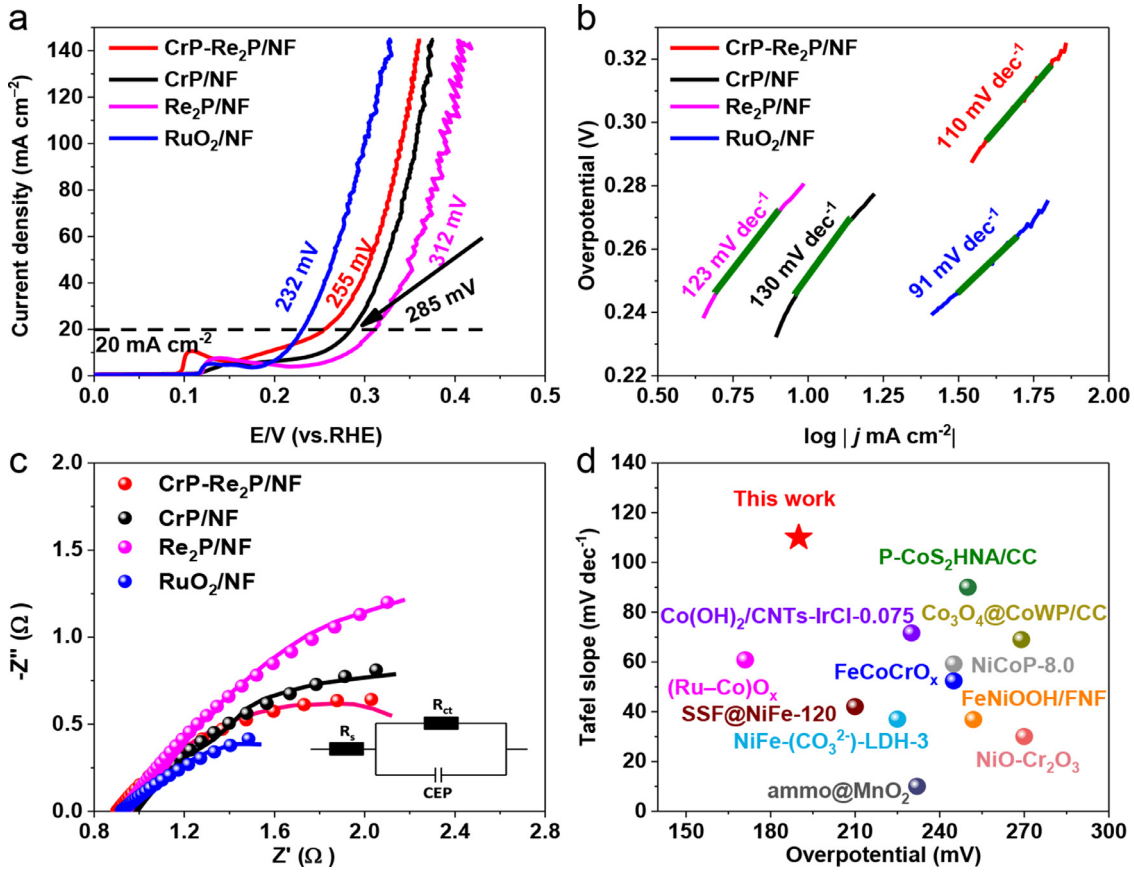

Fig. 5. OER performance of the different catalysts in 1.0 M KOH. (a) LSV curves obtained at a scan rate of 0.2 mV s^{-1}, (b) corresponding Tafel slopes, (c) electrochemical impedance spectroscopy (EIS), and (d) comparison with the overpotentials of recently reported catalysts for OER activity at 20 mA cm^{-2}.

gesting a synergy between Cr and *Re*, which is the inherent reason for the excellent performance.

At the same time, CrP-Re_2P/NF also shows the lowest charge transfer impedance (R_{ct}) indicating that the CrP-Re_2P/NF composite has higher conductivity to promote charge transfer thereof better HER performance (Fig. S13) [47]. Remarkably, the CrP-Re_2P/NF is also dramatically outperformed most nonprecious metal catalysts reported recently (Fig. 4f and Table S4). Studies show that the superior HER performance of the catalyst at high current densities is closely related to the self-supporting nanostructures [48].

Meanwhile, the CrP-Re_2P/NF catalyst also demonstrated an excellent OER activity under alkaline conditions. Fig. 5a shows that CrP-Re_2P/NF afforded a current density of 20 mA cm^{-2} with an overpotential of 255 mV, which is much lower than those of CrP/NF (285 mV), Re_2P/NF (312 mV), and RuO_2/NF (232 mV) in 1.0 M KOH. Moreover, compared with CrP/NF and Re_2P/NF, CrP-Re_2P/NF also showed better OER mass activity at an overpotential of 300 mV (Fig. S10b). Fig. 5b displays the Tafel slope of the catalysts. The Tafel slope of CrP-Re_2P/NF is 110 mV dec^{-1} is comparable with RuO_2 (91 mV dec^{-1}) and lower than those of CrP/NF (130 mV dec^{-1}) and Re_2P/NF (123 mV dec^{-1}) evidencing that CrP-Re_2P/NF has a fast reaction kinetic [49,50]. The EIS in Fig. 5c also illustrates that the CrP-Re_2P/NF has better conductivity than all the control catalysts to promote faster electron transfer [51]. Fig. 5d and Table S5 summarize the state-of-the-art OER performance of electrocatalysts in 1.0 M KOH, where the overpotential of CrP-Re_2P/NF is lower than that of most transition metal catalysts.

To further demonstrate the bifunctional performance of the catalyst, we also assembled an electrolytic cell for overall water splitting (Fig. 6a) [52]. The test was performed using CrP-Re_2P/NF as a bifunctional cathode and anode catalysts in a two-electrode system in 30% KOH solution (Fig. 6b) and 1.0 M KOH (Fig. S14). Note that 30% KOH was chosen because this concentration is commonly used in commercial applications [32]. For comparison, we used Pt/C/NF and RuO_2/NF as the cathode and anode under the same conditions, respectively. Obviously, the LSV polarization curve shows that CrP-Re_2P/NF cell can reach 500 mA cm^{-2} only with a potential of 1.89 V, in line with the RuO_2/NF $^{(+)}$ || Pt/C/NF $^{(-)}$ cell. When reaching 1000 mA cm^{-2}, the required potential is 2.02 V, which is lower than the RuO_2/NF $^{(+)}$ || Pt/C/NF $^{(-)}$ cell (2.05 V). The recently reported high-performance catalysts in a two-electrode system in 1.0 M KOH are summarized in Fig. 6c and Table S6. It can observe that the bifunctional CrP-Re_2P/NF $^{(+/-)}$ catalyst is similar or surpassing most of the catalysts reported at 100 mA cm^{-2} in the two-electrode system. As shown in Fig. 6d, the stability test was performed in a two-electrode system in 30% KOH. The catalyst also exhibits outstanding stability as no degradation was observed for 100 h of continues operation at 100 mA cm^{-2} current density.

In addition, the long-term stability test of CrP-Re_2P/NF was further carried out at the constant current density. Fig. S15 illustrates that both overpotentials of HER and OER CrP-Re_2P/NF show no significant increase after 100 h at the current density of 100 mA cm^{-2}, suggesting high HER and OER stabilities. Meanwhile, the polarization curve after 3000 CV cycles is almost the same as at the beginning, which further confirms the excellent stability of CrP-Re_2P/NF (Fig. S16).

Furthermore, the XRD pattern of CrP-Re_2P/NF shows the original structural composition after 100 h of HER stability. At the same time, only a few distinct peaks are left after OER stability (Fig. S17), indicating the oxidation of phosphides. The SEM images reveal that

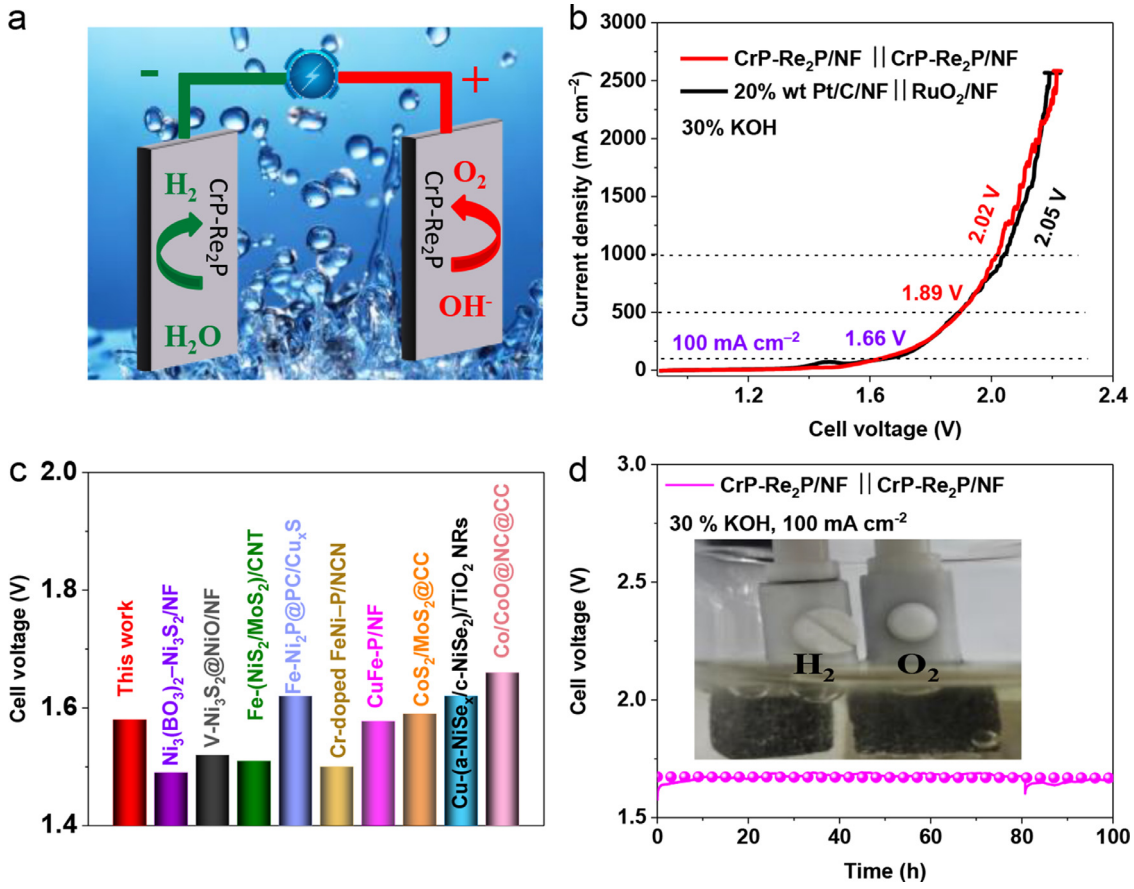

Fig. 6. (a) The schematic diagram of overall water splitting electrolyzer using CrP-Re_2P/NF as bifunctional catalyst. (b) Comparison of polarization curves of CrP-Re_2P/NF $^{(+/-)}$ and the RuO_2/NF $^{(+)}$||20 wt%Pt/C/NF $^{(-)}$ at high currents in 30 wt% KOH. (c) Comparing cell voltages with the newly reported electrolyzers at 100 mA cm^{-2} in 1.0 M KOH. (d) Durability test of CrP-Re_2P/NF $^{(+/-)}$ at 100 mA cm^{-2} in 30 wt% KOH.

the surface show more aggregation after OER but there is no clear change after HER (Fig. S18). XPS analysis exhibits that the original elemental composition has remained after HER because the HER is the electron-rich reduction process (Fig. S19). On the other hand, the phosphide peaks are disappeared, and the metal phosphides become Cr_2O_3/CrOOH and ReO_2 after OER due to the strong oxidation environment [53].

The alkaline Zn-H_2O cell based on CrP-Re_2P/NF electrode was established.As shown in Fig. 7a, zinc sheet is employed as the anode, 0.6 M KOH and 0.2 M $Zn(Ac)_2$ solution is served as the electrolyte to assemble the Zn-H_2O cell to achieve simultaneous hydrogen evolution and power generation [54]. When the cell starts to discharge, the HER reaction will proceed on the cathode to produce H_2, meanwhile the zinc plate is oxidized on the anode. The Zn-H_2O cell based on CrP-Re_2P/NF provides a high open circuit voltage of 1.04 V as shown in Fig. 7b. The CrP-Re_2P/NF-based Zn-H_2O cell can reach a power density of 8.8 mW cm^{-2}, which is superior to commercial Pt/C-based Zn-H_2O cell (Fig. 7c). Furthermore, two Zn-H_2O cells connected in series can light up a red light-emitting diode (the power rating of a LED is 30 mW) shows in Fig. 7d, which reveals the potential application prospect of zinc-based energy. The CrP-Re_2P/NF-based Zn-H_2O cell shows a lower discharge voltage and long-term stability of over 180 h at a current density of 10 mA cm^{-2}, indicating that the CrP-Re_2P/NF catalyst possesses potential application in the Zn-H_2O cell (Fig. 7e). It's worth noting that the several voltage leaps in the long-term stability test can be seen in Fig. 7e. This is due to a period of stability testing, the surface of CrP-Re_2P/NF and Zn sheet were covered with ZnO, which seriously hindered the progress of the reaction. Therefore, the ZnO was removed from the catalyst surface by rinsing with deionized water and 0.5 M H_2SO_4, respectively, and the washed CrP-Re_2P/NF continued to be used as a cathode catalyst to assemble the Zn-H_2O cell and test the stability (Fig. S20). Since its stability is tested after a few flushes, several voltage leaps occur during the long-term stability test [54,55].

As discussing above, the excellent electrocatalytic performance of CrP-Re_2P/NF for HER/OER in alkaline electrolytes can be attributed to the following three aspects:(1) The porous structure with high conductivity can provide a large electrochemically active surface area and expose more active sites to improve electrocatalytic activity [56,57]; (2) There is a strong electronic interaction between CrP and Re_2P components, which results in a partial negative charge on Re_2P and a partial positive charge on CrP species [32]. In alkaline medium for HER, an electron is obtained at the interface of the two components, which promotes the dissociation of H_2O and forms the adsorbed H* and OH* intermediates on CrP and Re_2P surfaces, respectively. XPS results show a robust electronic interaction between CrP and Re_2P, and the electron is transferred from Re_2P to CrP, which made it favorable towards OH* adsorption on *Re* species and the adsorption of H* on the CrP surface. Subsequently, the adsorped H* on CrP surface interacts with another H_2O molecule and obtains an electron simultaneously, thus forming a H_2 molecule and liberating a new active site for the next cycle [58]; (3) According to most of previous works, the transition metal phosphide is a pre-catalyst for OER in alkaline medium. A thin layer of oxide or oxyhydroxide is formed on the surface of the catalysts as the active center in the OER process [53,59]. The resulted hybrid structure can regulate the binding energies of OER

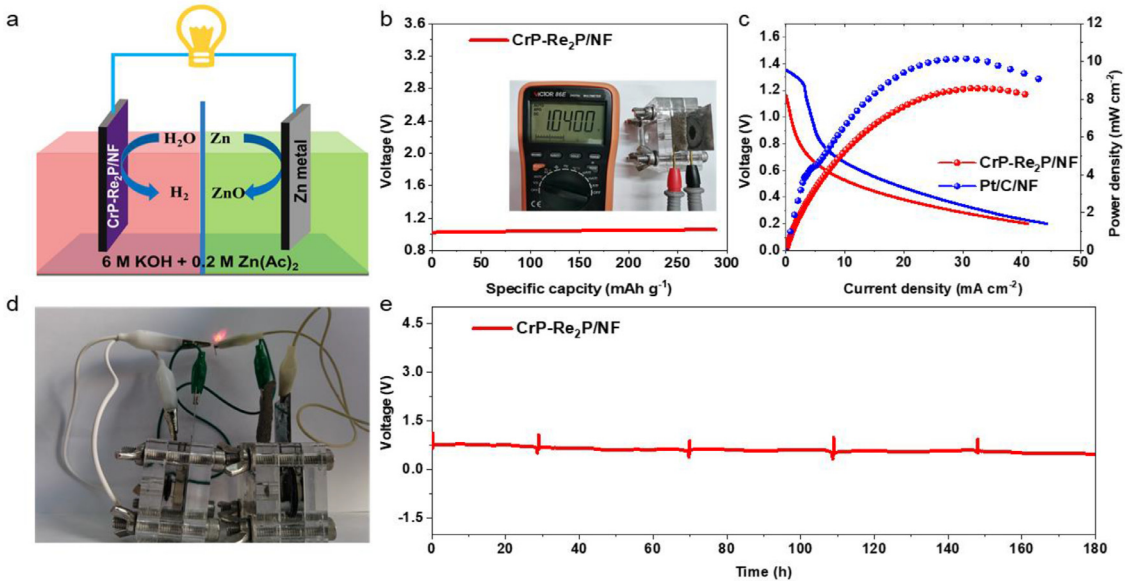

Fig. 7. (a) The schematic diagram of Zn-H_2O cell. (b) Open-circuit plots of Zn-H_2O cell assembled with CrP-Re_2P/NF and the photo of the open circuit voltage tested by the meter. (c) The polarization curve and power density of CrP-Re_2P/NF and Pt/C/NF. (d) Digital graph of a single red LED lighted by two series of CrP-Re_2P/NF-based Zn-H_2O cell. (e) Long-term durability test at a current density of 10 mA cm^{-2} of Zn-H_2O cell using CrP-Re_2P/NF as cathode.

intermediates, thereby synergistically enhancing OER catalytic activity [60,61].

4. Conclusion

In summary, we have successfully fabricated CrP-Re_2P/NF electrocatalyst with rich porous nanostructures, which exhibited impressive bifunctional activity and super stability in alkaline water splitting. More importantly, the CrP-Re_2P/NF can provide high current densities of 500 and 1000 mA cm^{-2} at 1.89 and 2.02 V in 30% KOH, respectively. In addition, CrP-Re_2P/NF reveals extraordinary durability of 100 h at 100 mA cm^{-2} in 30% KOH with negligible degradation in overall water splitting. Moreover, the alkaline Zn-H_2O cell was fabricated with CrP-Re_2P/NF as the cathode, which can deliver a power density of 8.8 mW cm^{-2} and long-term stability of more than 180 h. The high activity and outstanding stability are attributed to the fast charge transfer and synergistic effect between CrP and Re_2P components. This work provides innovative ideas and methods for constructing efficient bifunctional catalysts at high current densities in energy conversion applications and industrial applications.

Appendix A. Supplementary data

Electronic supplementary information (ESI) available. See DOI: 10.1016/j.electacta.2021.xxxxxx

CRediT authorship contribution statement

Lixia Wang: Writing – review & editing, Methodology, Investigation. **Zhiyang Huang:** Investigation, Data curation. **Hexiu Huang:** Data curation. **Shenghong Zhong:** Investigation, Data curation. **Meiling Huang:** Methodology. **Tayirjan Taylor Isimjan:** Writing – review & editing. **Xiulin Yang:** Supervision, Writing – review & editing.

Declaration of Competing Interest

The authors declare that they have no known competing financial interests or personal relationships that could have appeared to influence the work reported in this paper.

Credit authorship contribution statement

Lixia Wang: Writing – review & editing, Methodology, Investigation. **Zhiyang Huang:** Investigation, Data curation. **Hexiu Huang:** Data curation. **Shenghong Zhong:** Investigation, Data curation. **Meilin Huang:** Methodology. **Tayirjan Taylor Isimjan:** Writing – review & editing. **Xiulin Yang:** Supervision, Writing – review & editing.

Acknowledgement

This work has been supported by the National Natural Science Foundation of China (No. 21965005), Natural Science Foundation of Guangxi Province (2018GXNSFAA294077, 2021GXNSFAA076001), Project of High-Level Talents of Guangxi (F-KA18015), Graduate Education Innovation Program (SA1900000403), and Guangxi Technology Base and Talent Subject (GUIKE AD18126001, GUIKE AD20297039).

Notes

There are no financial interests or personal relationships to influence the work.

Supplementary materials

Supplementary material associated with this article can be found, in the online version, at doi:10.1016/j.electacta.2021.139598.

References

[1] L. Yang, H. Li, Y. Yu, Y. Wu, L. Zhang, Assembled 3D MOF on 2D nanosheets for self-boosting catalytic synthesis of N-doped carbon nanotube encapsulated metallic co electrocatalysts for overall water splitting, Appl. Catal. B Environ. 271 (2020) 118939.
[2] H. Hosseini, M. Roushani, Rational design of hollow core-double shells hybrid nanoboxes and nanopipes composed of hierarchical Cu-Ni-Co selenides anchored on nitrogen-doped carbon skeletons as efficient and stable bifunctional electrocatalysts for overall water splitting, Chem. Eng. J. 402 (2020) 126174.
[3] J. Wu, T. Chen, C. Zhu, J. Du, L. Huang, J. Yan, D. Cai, C. Guan, C. Pan, Rational construction of a WS_2/CoS_2 heterostructure electrocatalyst for efficient hydrogen evolution at all pH values, ACS Sustain. Chem. Eng. 8 (2020) 4474–4480.

[4] B. Li, Z. Li, Q. Pang, J.Z. Zhang, Core/shell cable-like Ni3S2 nanowires/N-doped graphene-like carbon layers as composite electrocatalyst for overall electrocatalytic water splitting, Chem. Eng. J. 401 (2020) 126045.

[5] B. Tang, X. Yang, Z. Kang, L. Feng, Crystallized $RuTe_2$ as unexpected bifunctional catalyst for overall water splitting, Appl. Catal. B Environ. 278 (2020) 119281.

[6] X. Liu, M. Gong, S. Deng, T. Zhao, J. Zhang, D. Wang, Recent advances on metal alkoxide-based electrocatalysts for water splitting, J. Mater. Chem. A 8 (2020) 10130–10149.

[7] C. Wang, L. Qi, Heterostructured inter-doped ruthenium-cobalt oxide hollow nanosheet arrays for highly efficient overall water splitting, Angew. Chem. Int. Ed. 59 (2020) 17219–17224.

[8] Z. Yan, H. Liu, Z. Hao, M. Yu, X. Chen, J. Chen, Electrodeposition of (hydro)oxides for an oxygen evolution electrode, Chem. Sci. 11 (2020) 10614–10625.

[9] Y. Chen, J. Yu, J. Jia, F. Liu, Y. Zhang, G. Xiong, R. Zhang, R. Yang, D. Sun, H. Liu, W. Zhou, Metallic Ni_3Mo_3N porous microrods with abundant catalytic sites as efficient electrocatalyst for large current density and superstability of hydrogen evolution reaction and water splitting, Appl. Catal. B Environ. 272 (2020) 118956.

[10] W. Ahn, G. Park Moon, U. Lee Dong, H. Seo Min, G. Jiang, P. Cano Zachary, M. Hassan Fathy, Z. Chen, Hollow multivoid nanocuboids derived from ternary Ni–Co–Fe prussian blue analog for dual-electrocatalysis of oxygen and hydrogen evolution reactions, Adv. Funct. Mater. 28 (2018) 1802129.

[11] N.U.A. Babar, Y.F. Joya, H. Khalil, F. Hussain, K.S. Joya, Thin-film iron-oxide nanobeads as bifunctional electrocatalyst for high activity overall water splitting, Int. J. Hydrog. Energy 46 (2021) 7885–7902.

[12] Y. Cheng, H. Guo, P. Yuan, X. Li, L. Zheng, R. Song, Self-supported bifunctional electrocatalysts with Ni nanoparticles encapsulated in vertical N-doped carbon nanotube for efficient overall water splitting, Chem. Eng. J. 413 (2020) 127531.

[13] B. Geng, F. Yan, L. Liu, C. Zhu, B. Li, Y. Chen, Ni/MoC heteronanoparticles encapsulated within nitrogen-doped carbon nanotube arrays as highly efficient self-supported electrodes for overall water splitting, Chem. Eng. J. 406 (2021) 126815.

[14] J. Luo, X. Qiao, J. Jin, X. Tian, H. Fan, D. Yu, W. Wang, S. Liao, N. Yu, Y. Deng, A strategy to unlock the potential of CrN as a highly active oxygen reduction reaction catalyst, J. Mater. Chem. A 8 (2020) 8575–8585.

[15] A. Falch, S.P. Babu, A review and perspective on electrocatalysts containing Cr for alkaline water electrolysis: hydrogen evolution reaction, Electrocatalysis 12 (2021) 104–116.

[16] X. Du, H. Su, X. Zhang, Cr doped-Co9S8 nanoarrays as high-efficiency electrocatalysts for water splitting, J. Alloy. Compd. 824 (2020) 153965.

[17] Y. Lin, Z. Tian, L. Zhang, J. Ma, Z. Jiang, B.J. Deibert, R. Ge, L. Chen, Chromium-ruthenium oxide solid solution electrocatalyst for highly efficient oxygen evolution reaction in acidic media, Nat. Commun. 10 (2019) 162.

[18] C.C. Lin, C.C.L. McCrory, Effect of chromium doping on electrochemical water oxidation activity by Co_3–$xCrxO_4$ spinel catalysts, ACS Catal. 7 (2017) 443–451.

[19] K. Li, X. Jian, S. Li, W. Wang, Y. Lei, P. Zhang, J. Liu, C. Zhou, L. Chen, *In situ* growth of urchin-like cobalt–chromium phosphide on 3D graphene foam for efficient overall water splitting, Inorg. Chem. Front. 7 (2020) 4913–4923.

[20] J. Liu, X. Yu, R. Du, C. Zhang, T. Zhang, J. Llorca, J. Arbiol, Y. Wang, M. Meyns, A. Cabot, Chromium phosphide CrP as highly active and stable electrocatalysts for oxygen electroreduction in alkaline media, Appl. Catal. B Environ. 256 (2019) 117846.

[21] L. An, J. Feng, Y. Zhang, R. Wang, H. Liu, G.C. Wang, F. Cheng, P. Xi, Epitaxial heterogeneous interfaces on N-$NiMoO_4$/NiS_2 nanowires/nanosheets to boost hydrogen and oxygen production for overall water splitting, Adv. Funct. Mater. 29 (2019) 1805298.

[22] J. Bao, Y. Zhou, Y. Zhang, X. Sheng, Y. Wang, S. Liang, C. Guo, W. Yang, T. Zhuang, Y. Hu, Engineering water splitting sites in three-dimensional flower-like Co–Ni–P/MoS_2 heterostructural hybrid spheres for accelerating electrocatalytic oxygen and hydrogen evolution, J. Mater. Chem. A 8 (2020) 22181–22190.

[23] F. Sun, Y. Wang, L. Fang, X. Yang, W. Fu, D. Tian, Z. Huang, J. Li, H. Zhang, Y. Wang, New vesicular carbon-based rhenium phosphides with all-pH range electrocatalytic hydrogen evolution activity, Appl. Catal. B Environ. 256 (2019) 117851.

[24] Z. Lai, A. Chaturvedi, Y. Wang, T.H. Tran, X. Liu, C. Tan, Z. Luo, B. Chen, Y. Huang, G.H. Nam, Z. Zhang, Y. Chen, Z. Hu, B. Li, S. Xi, Q. Zhang, Y. Zong, L. Gu, C. Kloc, Y. Du, H. Zhang, Preparation of 1T'-Phase ReS2xSe21-($_x$ = 0–1) nanodots for highly efficient electrocatalytic hydrogen evolution reaction, J. Am. Chem. Soc. 140 (2018) 8563–8568.

[25] Y. Zhou, E. Song, J. Zhou, J. Lin, R. Ma, Y. Wang, W. Qiu, R. Shen, K. Suenaga, Q. Liu, J. Wang, Z. Liu, J. Liu, Auto-optimizing hydrogen evolution catalytic activity of ReS_2 through intrinsic charge engineering, ACS Nano 12 (2018) 4486–4493.

[26] J. Qi, J. Finzel, H. Robatjazi, M. Xu, A.S. Hoffman, S.R. Bare, X. Pan, P. Christopher, Selective methanol carbonylation to acetic acid on heterogeneous atomically dispersed ReO_4/SiO_2 catalysts, J. Am. Chem. Soc. 142 (2020) 14178–14189.

[27] J. Aliaga, P. Vera, J. Araya, L. Ballesteros, J. Urzua, M. Farias, F. Paraguay-Delgado, G. Alonso-Nunez, G. Gonzalez, E. Benavente, Electrochemical hydrogen evolution over hydrothermally synthesized *Re*-doped MoS_2 flower-like microspheres, Molecules 24 (2019) 4631.

[28] Y. Gao, Y. Zhao, H. Liu, M. Shao, Z. Chen, T. Ma, Z. Wu, L. Wang, P-doped N, carbon supported ruthenium doped Rhenium phosphide with porous nanostructure for hydrogen evolution reaction using sustainable energies, J. Colloid Interface Sci. 606 (2022) 1874–1881.

[29] Y. Moon, D. Lee, Corrosion resistance of 316 L stainless steel with surface layer of Ni_2Al_3 or NiAl in molten carbonates, J. Power Sources 115 (2003) 1–11.

[30] J. Zhao, X. Ren, X. Sun, Y. Zhang, Q. Wei, X. Liu, D. Wu, *In situ* evolution of surface Co_2CrO_4 to CoOOH/CrOOH by electrochemical method: toward boosting electrocatalytic water oxidation, Chin. J. Catal. 42 (2021) 1096–1101.

[31] W. Cui, P. Li, Y. Chen, C. Liu, H. Zhang, S. Wang, H. Wang, S. Zheng, Y. Zhang, Preparation of high quality microgranulate CrO_3 based on green process design, Can. J. Chem. Eng. 95 (2017) 1261–1268.

[32] B. Wang, H. Huang, T. Sun, P. Yan, T.T. Isimjan, J. Tian, X. Yang, Dissolution reconstruction of electron-transfer enhanced hierarchical NiS_x-MoO_2 nanosponges as a promising industrialized hydrogen evolution catalyst beyond Pt/C, J. Colloid Interface Sci. 567 (2020) 339–346.

[33] J. Guo, B. Wang, D. Yang, Z. Wan, P. Yan, J. Tian, T.T. Isimjan, X. Yang, Rugae-like Ni_2P-CoP nanoarrays as a bi-functional catalyst for hydrogen generation: naBH4 hydrolysis and water reduction, Appl. Catal. B Environ. 265 (2020) 118584.

[34] A. Bumajdad, S. Al-Ghareeb, M. Madkour, F.A. Sagheer, Non-noble,efficient catalyst of unsupported alpha-Cr_2O_3 nanoparticles for low temperature CO oxidation, Sci. Rep. 7 (2017) 14788.

[35] E. Benavente, J.A. Aliaga, P. Barraza, J.F. Araya, M.H. Farías, G. González, G. Alonso-Núñez, Melamine-assisted synthesis of nitrogen-doped ReS_2 nanosheets/carbon composites, Mater. Lett. 243 (2019) 42–45.

[36] S. Oktay, Z. Kahraman, M. Urgen, K. Kazmanli, XPS investigations of tribolayers formed on TiN and (Ti,*Re*)N coatings, Appl. Surf. Sci. 328 (2015) 255–261.

[37] L. Wu, L. Yu, F. Zhang, B. McElhenny, D. Luo, A. Karim, S. Chen, Z. Ren, Heterogeneous bimetallic phosphide Ni_2P-Fe_2P as an efficient bifunctional catalyst for water/seawater splitting, Adv. Funct. Mater. 31 (2020) 2006484.

[38] H. Liu, J. Guan, S. Yang, Y. Yu, R. Shao, Z. Zhang, M. Dou, F. Wang, Q. Xu, Metal-organic framework-derived Co_2P nanoparticle/multi-doped porous carbon as a trifunctional electrocatalyst, Adv. Mater. 32 (2020) 202003649.

[39] M. Li, X. Liu, Y. Xiong, X. Bo, Y. Zhang, C. Han, L. Guo, Facile synthesis of various highly dispersive CoP nanocrystal embedded carbon matrices as efficient electrocatalysts for the hydrogen evolution reaction, J. Mater. Chem. A 3 (2015) 4255–4265.

[40] L. Yang, L. Huang, Y. Yao, L. Jiao, *In-situ* construction of lattice-matching NiP_2/$NiSe_2$ heterointerfaces with electron redistribution for boosting overall water splitting, Appl. Catal. B Environ. 282 (2021) 119584.

[41] L. Yang, R. Liu, L. Jiao, Electronic redistribution: construction and modulation of interface engineering on CoP for enhancing overall water splitting, Adv. Funct. Mater. 30 (2020) 1909618.

[42] N. Yao, R. Meng, F. Wu, Z. Fan, G. Cheng, W. Luo, Oxygen-vacancy-induced CeO_2/Co_4N heterostructures toward enhanced pH-universal hydrogen evolution reactions, Appl. Catal. B Environ. 277 (2020) 119282.

[43] D.T. Tran, H.T. Le, V.H. Hoa, N.H. Kim, J.H. Lee, Dual-coupling ultrasmall iron-Ni_2P into P-doped porous carbon sheets assembled CuxS nanobrush arrays for overall water splitting, Nano Energy 84 (2021) 105861.

[44] A. Wu, Y. Gu, B. Yang, H. Wu, H. Yan, Y. Jiao, D. Wang, C. Tian, H. Fu, Porous cobalt/tungsten nitride polyhedra as efficient bifunctional electrocatalysts for overall water splitting, J. Mater. Chem. A 8 (2020) 22938–22946.

[45] S. Shen, Z. Lin, K. Song, Z. Wang, L. Huang, L. Yan, F. Meng, Q. Zhang, L. Gu, W. Zhong, Reversed active sites boost the intrinsic activity of graphene–like cobalt selenide for hydrogen evolution, Angew. Chem. Int. Ed. 60 (2021) 12360–12365.

[46] Y. Hu, H. Yu, L. Qi, J. Dong, P. Yan, T. Taylor Isimjan, X. Yang, Interface engineering of needle-like P-doped MoS_2/CoP arrays as highly active and durable bifunctional electrocatalyst for overall water splitting, ChemSusChem 14 (2021) 1565–1573.

[47] F. Luo, L. Guo, Y. Xie, J. Xu, K. Qu, Z. Yang, Iridium nanorods as a robust and stable bifunctional electrocatalyst for pH-universal water splitting, Appl. Catal. B Environ. 279 (2020) 119394.

[48] L. Ye, J. Wang, Y. Zhang, M. Zhang, X. Jing, Y. Gong, A self-supporting electrode with *in-situ* partial transformation of Fe-MOF into amorphous NiFe-LDH for efficient oxygen evolution reaction, Appl. Surf. Sci. 556 (2021) 149781.

[49] C. Qiang, M. Liu, L. Zhang, Z. Chen, Z. Fang, *In situ* growth of Ni-based metal–organic framework nanosheets on carbon nanotube films for efficient oxygen evolution reaction, Inorg. Chem. 60 (2021) 3439–3446.

[50] C. Chen, Y. Tuo, Q. Lu, H. Lu, S. Zhang, Y. Zhou, J. Zhang, Z. Liu, Z. Kang, X. Feng, D. Chen, Hierarchical trimetallic Co-Ni-Fe oxides derived from core-shell structured metal-organic frameworks for highly efficient oxygen evolution reaction, Appl. Catal. B Environ. 287 (2021) 119953.

[51] L. Wang, Z. Li, K. Wang, Q. Dai, C. Lei, B. Yang, Q. Zhang, L. Lei, M.K.H. Leung, Y. Hou, Tuning D-band center of tungsten carbide via Mo doping for efficient hydrogen evolution and Zn–H_2O cell over a wide pH range, Nano Energy 74 (2020) 104850.

[52] C.N. Lv, L. Zhang, X.H. Huang, Y.X. Zhu, X. Zhang, J.S. Hu, S.Y. Lu, Double functionalization of N-doped carbon carved hollow nanocubes with mixed metal phosphides as efficient bifunctional catalysts for electrochemical overall water splitting, Nano Energy 65 (2019) 103995.

[53] O. Neumann, A.D. Neumann, S. Tian, C. Thibodeaux, S. Shubhankar, J. Müller, E. Silva, A. Alabastri, S.W. Bishnoi, P. Nordlander, N.J. Halas, Combining solar steam processing and solar distillation for fully off-grid production of cellulosic bioethanol, ACS Energy Lett. 2 (2017) 8–13.

[54] F. Cheng, L. Wang, H. Wang, C. Lei, B. Yang, Z. Li, Q. Zhang, L. Lei, S. Wang, Y. Hou, Boosting alkaline hydrogen evolution and Zn–H_2O cell induced by interfacial electron transfer, Nano Energy 71 (2020) 104621.

[55] Y. Pei, S. Guo, Q. Ju, Z. Li, P. Zhuang, R. Ma, Y. Hu, Y. Zhu, M. Yang, Y. Zhou,

J. Shen, J. Wang, Interface engineering with ultralow ruthenium loading for efficient water splitting, ACS Appl. Mater. Interfaces 12 (2020) 36177–36185.
[56] D. Li, C. Zhou, R. Yang, Y. Xing, S. Xu, D. Jiang, D. Tian, W. Shi, Interfacial engineering of the CoxP–Fe_2P heterostructure for efficient and robust electrochemical overall water splitting, ACS Sustain. Chem. Eng. 9 (2021) 7737–7748.
[57] D. Chen, R. Lu, Z. Pu, J. Zhu, H.W. Li, F. Liu, S. Hu, X. Luo, J. Wu, Y. Zhao, S. Mu, Ru-doped 3D flower-like bimetallic phosphide with a climbing effect on overall water splitting, Appl. Catal. B Environ. 279 (2020) 119396.
[58] Y. Song, J. Cheng, J. Liu, Q. Ye, X. Gao, J. Lu, Y. Cheng, Modulating electronic structure of cobalt phosphide porous nanofiber by ruthenium and nickel dual doping for highly-efficiency overall water splitting at high current density, Appl. Catal. B Environ. 298 (2021) 120488.
[59] L.A. Stern, L. Feng, F. Song, X. Hu, Ni2P as a Janus catalyst for water splitting: the oxygen evolution activity of Ni_2P nanoparticles, Energy Environ. Sci. 8 (2015) 2347–2351.
[60] Z. Chen, R. Zheng, M. Graś, W. Wei, G. Lota, H. Chen, B.J. Ni, Tuning electronic property and surface reconstruction of amorphous iron borides via W-P co–doping for highly efficient oxygen evolution, Appl. Catal. B: Environ. 288 (2021) 120037.
[61] T. Zhao, X. Shen, Y. Wang, R.K. Hocking, Y. Li, C. Rong, K. Dastafkan, Z. Su, C. Zhao, *In situ* reconstruction of V-doped Ni_2P pre-catalysts with tunable electronic structures for water oxidation, Adv. Funct. Mater. 31 (2021) 2100614.